Self-construction of actin networks through phase separation–induced abLIM1 condensates

Sen Yang[a,b,1], Chunxia Liu[b,c,1], Yuting Guo[d], Guoqing Li[a,b], Dong Li[d], Xiumin Yan[a] (ORCID), and Xueliang Zhu[a,b,c,e,2] (ORCID)

The abLIM1 is a nonerythroid actin-binding protein critical for stable plasma membrane–cortex interactions under mechanical tension. Its depletion by RNA interference results in sparse, poorly interconnected cortical actin networks and severe blebbing of migrating cells. Its isoforms, abLIM-L, abLIM-M, and abLIM-S, contain, respectively four, three, and no LIM domains, followed by a C terminus entirely homologous to erythroid cortex protein dematin. How abLIM1 functions, however, remains unclear. Here we show that abLIM1 is a liquid–liquid phase separation (LLPS)-dependent self-organizer of actin networks. Phase-separated condensates of abLIM-S-mimicking ΔLIM or the major isoform abLIM-M nucleated, flew along, and cross-linked together actin filaments (F-actin) to produce unique aster-like radial arrays and interconnected webs of F-actin bundles. Interestingly, ΔLIM condensates facilitated actin nucleation and network formation even in the absence of Mg^{2+}. Our results suggest that abLIM1 functions as an LLPS-dependent actin nucleator and cross-linker and provide insights into how LLPS-induced condensates could self-construct intracellular architectures of high connectivity and plasticity.

actin polymerization | liquid–liquid phase separation | cell cortex | F-actin networks | self-construction

Actin filaments are nucleated and cross-linked into diverse regional networks for different cellular functions. The well-documented erythroid cortex is a plasma membrane–anchored polygonal meshwork consisting of spectrin tetramers cross-linked at nodes by short actin filaments and other actin-binding proteins such as dematin and adducin (1, 2). In contrast, nonerythroid cortexes are mostly actin-based irregular architectures composed regionally of dynamic webs and bundles, and rays of F-actin. They exert a wide variety of cellular activities, including mechanical tension, migration, morphogenesis, blebbing, and endocytosis (1–8). Notably, recent atomic force microscopy and superresolution fluorescent microscopy have frequently spotted varying numbers of aster-like radial cortical actin arrays (9–12). Formations of cortical actin arrays such as stress fibers and lamellipodia are well studied and attributed to formins and the Arp2/3 complex, nucleators of linear and branched actin filaments, respectively (7, 13–16). Nevertheless, these classical actin nucleators do not appear to account for the formation of all cortical actin (17). How other cortical actin arrays, including the asters, are constructed also remains unclear.

Proteins can phase separate through intermolecular interactions into biomolecular condensates that underlie the formation of nonmembranous organelles and other compartmented subcellular structures, including cytoskeletal networks (18–22). The liquid–liquid phase separation (LLPS) of microtubule-binding proteins, for instance, induces radial or bundled microtubule arrays by concentrating tubulin (23–26). In contrast, only signaling proteins have been shown to undergo LLPS to recruit activators of the Arp2/3 complex for the construction of cortical actin networks at the leading edge or cell–cell junctions (27–29). Although G-actin can polymerize into F-actin spontaneously at high concentrations in vitro, it requires the aid of nucleators to produce initial actin dimers or trimers for efficient polymerization in vivo (7, 15, 16). As LLPS of proteins generates condensates abundant in their active domains to function potentially as reaction centers and may also endow them with properties absent in the individual molecules, we speculated that LLPS might transform proteins into condensates capable of polymerizing and organizing unique actin arrays.

The abLIM1 is an actin-bundling protein with a C-terminal region sharing ∼40% of identity with the entire dematin (30, 31), which consists of a large N-terminal intrinsically disordered region (IDR) and a short actin-binding villin headpiece (VHP) domain (32–35). The abLIM1 is expressed as three isoforms based on messenger RNA (mRNA) transcript analysis (30). The long one (abLIM-L, expressed exclusively in retinal rod cells), the middle one (abLIM-M, the widely expressed major isoform), and the short one (abLIM-S, the dematin-like isoform) respectively contain four, three, and no

Significance

Actin filaments (F-actin) are polymerized from monomeric globular actin (G-actin) to form regional networks for various functions through interplays of actin nucleating and cross-linking proteins. Cortical actin networks, for instance, are assembled underneath and anchored to the plasma membrane. Cortexes of most cell types are mingled with dynamic linear fibers, aster-like radial arrays, and interconnected webs of F-actin. The abLIM1 is an F-actin-cross-linking protein that ensures the formation of dense cortical actin meshwork for cells to resist mechanical tension-induced blebbing. Here we show that it functions as a phase separation–dependent actin nucleator and cross-linker to self-construct radial arrays and highly interconnected meshwork of F-actin bundles.

[1]S.Y. and C.L. contributed equally to this work.

[2]To whom correspondence may be addressed. Email: xlzhu@sibcb.ac.cn.

N-terminal LIM domains, which function mainly for protein–protein interaction (36). Interestingly, abLIM1 and dematin are important for stable plasma membrane-to-cortex attachment of nonerythroid cells (31) and erythrocytes (33, 37, 38), respectively. Similar to dematin (37), the dematin-homologous region of abLIM1 also associates with spectrin and adducin, as shown through a construct (ΔLIM) mimicking abLIM-S (31). The depletion of abLIM1 by RNA interference (RNAi) abolishes the dense interconnected cortical actin meshwork, resulting in severe blebbing during cell spreading and free migration (31). The depletion also represses lamellipodial formation and directional cell migration (39). In this study, we demonstrate that abLIM1 functions through its dematin-homologous region as an LLPS-dependent self-organizer of asters and interconnected meshwork of actin bundles.

Results

Different Isoforms of abLIM1 Are Able to Decorate Radial F-actin Arrays in Cultured Cells. Although human abLIM1 had more than 20 isoforms according to the National Center for Biotechnology Information database, they could still be classified into the abLIM-L, abLIM-M, and abLIM-S groups (Fig. 1A and *SI Appendix*, Fig. S1) (30). Among them, abLIM-M, the most commonly expressed major isoform (30), had only one known mRNA transcript (*SI Appendix*, Fig. S1). Consistently, we have previously shown that, in U2OS and RPE1 cells, our anti-abLIM1 antibody mainly recognizes a band of ~80 kDa (apparent molecular weight) that can be depleted by abLIM1-specific small interference RNAs (siRNAs) abL1-i1 and abL1-i2 (Fig. 1B) (31, 39). To further clarify this, we expressed in cells Flag-tagged abLIM-L, abLIM-M, and the abLIM-S-mimicking ΔLIM (Fig. 1A) (31) and compared their mobilities in sodium dodecyl sulfate polyacrylamide gel electrophoresis (SDS/PAGE) with that of the endogenous protein (Fig. 1B). Indeed, the endogenous protein displayed motility similar to abLIM-M (Fig. 1B). To avoid confusion, we only used abLIM1 as a collective name in the following text.

Radial F-actin arrays have been shown to emerge at both the ventral and dorsal sides of cortical actin networks (9–11). Consistent with our previous report on abLIM-L and ΔLIM (31), exogenous abLIM-M also prominently decorated F-actin arrays (Fig. 1C). Interestingly, all three constructs were observed to decorate radial F-actin arrays and thus displayed aster-like distributions in confocal microscopy, three-dimensional structured illumination microscopy (3D-SIM), or recently developed cutting-edge grazing incidence SIM (GI-SIM) (Fig. 1 C–E), which generated superresolution (~100 nm) images covering a depth of ~1 μm at the ventral side of cells (40). These results imply a role of abLIM1 in the formation of radial F-actin arrays in addition to the dense interconnected cortical actin networks (31).

ΔLIM Autonomously Assembles Asters and Webs of F-actin Bundles In Vitro. We have previously shown that bacterially expressed His-tagged GFP-ΔLIM (3 μM) induces dense networks of bundled F-actin in vitro (31), similar to dematin (32). Consistent with the observations in cells (Fig. 1 C and D), we noticed that F-actin preparations produced with newly purified His-GFP-ΔLIM (*SI Appendix*, Fig. S2A) through the same protocol (Fig. 2A) also contained asters of ~10 μm in diameter (Fig. 2B). The asters usually contained an amorphous core positive for His-GFP-ΔLIM, from which numerous actin fibers decorated with GFP-ΔLIM protruded radially away (Fig. 2 B and C). Asters also emerged in 1 μM and even 0.1 μM GFP-ΔLIM,

but with increasingly reduced sizes (Fig. 2B). In 6 μM GFP-ΔLIM, asters were still observed outside or within clusters of intertwining F-actin networks (Fig. 2B). The astral actin filaments were generally much shorter than surrounding sporadic actin filaments in the same samples. GFP-ΔLIM decorated both astral and sporadic actin filaments at high (3 μM to 6 μM) concentrations but mainly the astral filaments at low (0.1 μM to 1 μM) concentrations (Fig. 2B), suggesting that the protein tends to function as a condensate. In comparison, actin filaments in 6 μM His-tagged GFP were randomly scattered and GFP-negative (Fig. 2B and *SI Appendix*, Fig. S2A) (31). Electron microscopy (EM) with negative staining revealed that the aster fibers contained tightly packed actin filaments, with an average diameter of 58.4 ± 0.9 nm ($n = 403$) (Fig. 2D). Therefore, ΔLIM condensates can serve as organizing centers for asters of bundled actin filaments in vitro.

To clarify whether the aster could be formed without preexisting F-actin, we performed the reactions in 35-mm glass-bottom Petri dishes and monitored a 6-μm-thick zone close to the bottom with a spinning disk microscope. To eliminate the possibility of preexisting F-actin, we directly mixed G-actin in the storage buffer (containing 0.2 mM CaCl₂ to suppress the polymerization) with GFP-ΔLIM (6 μM), followed by the addition of actin polymerization buffer. We used low concentrations of phalloidin-TRITC (tetramethylrhodamine B isothiocyanate) (4 μM final concentration) (41) to visualize F-actin (Fig. 2E). We observed that actin bundles decorated by GFP-ΔLIM, especially punctate GFP-ΔLIM condensates, emerged gradually after proximately 15 min and rapidly expanded over time into increasingly dense webs containing asters (Fig. 2F). The webs were quite stable, because they lasted for hours without signs of disassembly. To make use of this property, we reacquired z-stack images from the same sample to cover a depth of 80 μm after the time-lapse imaging was accomplished. We found that the dense web was ~6 μm to 7 μm thick and situated over an array of His-GFP-ΔLIM condensates at the bottom of the substratum, whereas numerous F-actin asters of varying size floated in the solution, along with sporadic bundles (Fig. 2G and Movie S1). To exclude the influence of the fluorescent dye, we also performed the experiments in the absence of phalloidin-TRITC and observed similar actin network formation (see Fig. 6F as an example). In comparison, when the reactions were similarly performed in 6 μM His-GFP, actin networks were not observed in live imaging (*SI Appendix*, Fig. S2B), possibly due to poor resolution on single actin filaments. Therefore, ΔLIM is able to self-organize asters and webs of actin bundles in vitro (Fig. 2H).

abLIM1 Undergoes LLPS through Its Dematin-Homologous Unfolded Region. The existence of ΔLIM condensates in astral centers (Fig. 2) prompted us to purify additional mutants (Fig. 3A and *SI Appendix*, Fig. S2A) to investigate whether abLIM1 functions through LLPS. As LLPS is temperature dependent (18–20, 22, 24), we compared purified GFP-ΔLIM in solutions stored on ice or incubated at 25 °C for 5 min and observed obvious turbidity of the incubated samples (Fig. 3B). Furthermore, the turbidity was reversible when the samples were shifted back and forth between 0 °C and 25 °C (Fig. 3B), resembling the reversible LLPS property of BuGZ (24). Microscopic examinations confirmed liquid droplet formation at temperatures that caused turbidity (Fig. 3C). The droplets increased both size and density in a concentration-dependent manner and could be clearly observed at 1-μM concentration (Fig. 3C). They could easily fuse into larger ones (Fig. 3D), confirming their liquid properties. Fluorescence recovery after photobleaching (FRAP) assays revealed
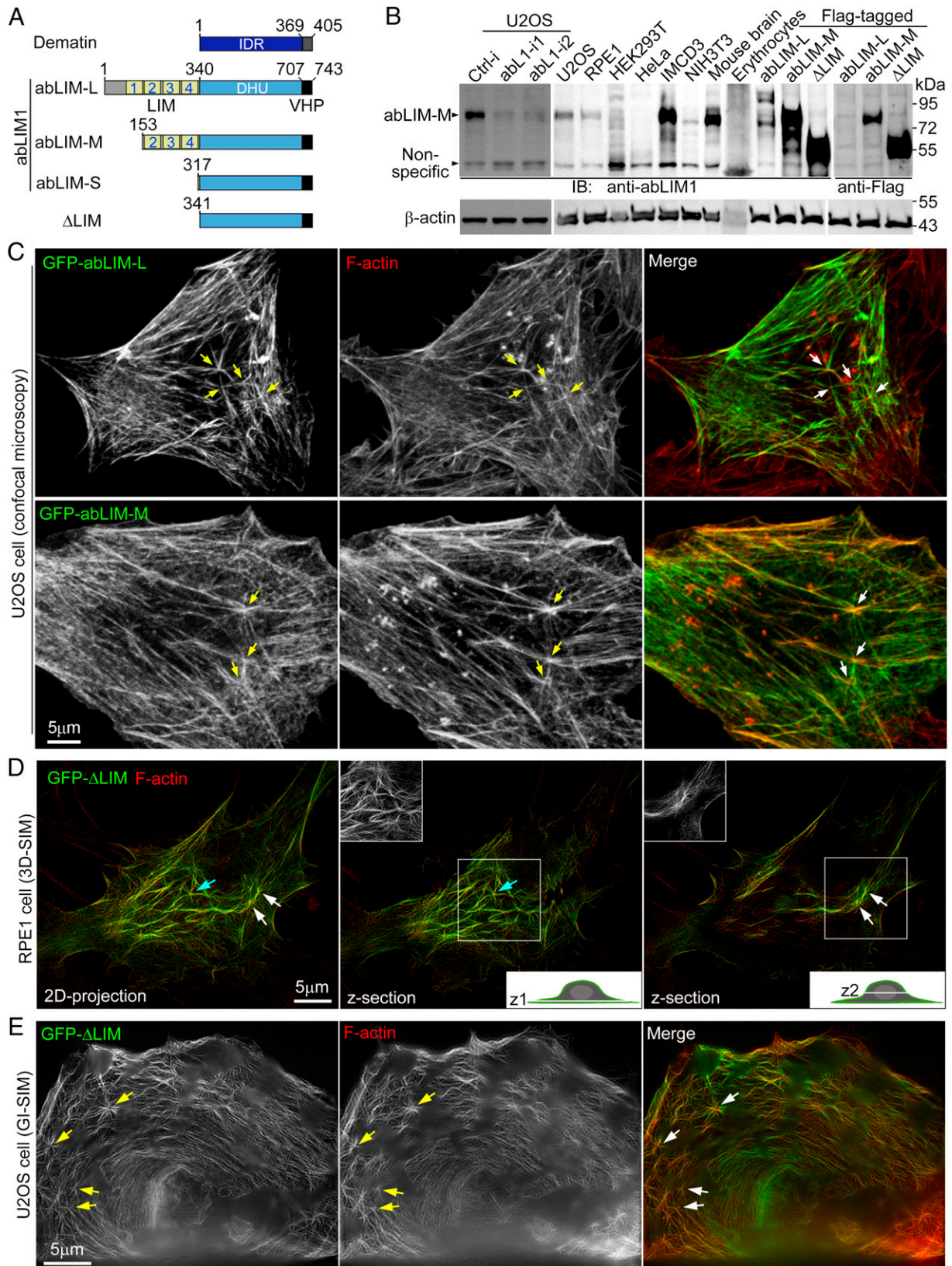
Fig. 1. The abLIM1 isoforms associate with subcellular actin cytoskeletons, including aster-like arrays. (*A*) Isoforms of human abLIM1. Isoforms used in this study have identical amino acid sequences in their overlapping regions. Refer to *SI Appendix*, Fig. S1 for details on different isoforms. The ΔLIM mutant, which was used to represent abLIM-S in this study, contains a dematin-homologous sequence. LIM, LIM domain-containing region. (*B*) The abLIM-M was a widely and predominantly expressed abLIM1 isoform. The position of endogenous abLIM1-specific band was validated by RNAi. Flag-tagged isoforms transiently expressed in intact RPE1 cells were used as size markers. β-actin served as a loading control. Ctrl-i, control siRNA; abL1-i1 and abL1-i2, two independent siRNAs against human abLIM1 (31); IB, immunoblotting. (*C–E*) Association of abLIM1 isoforms with actin networks. Cells expressing GFP-tagged constructs of abLIM1 were stained with phalloidin-TRITC to label F-actin and imaged with confocal microscopy (*C*), 3D-SIM (*D*), or GI-SIM (*E*). The framed regions in *D* show the GFP channel. Arrows point to typical F-actin-based astral arrays. The cyan and white arrows in *D* point to typical astral arrays at the ventral side and the dorsal site, respectively.
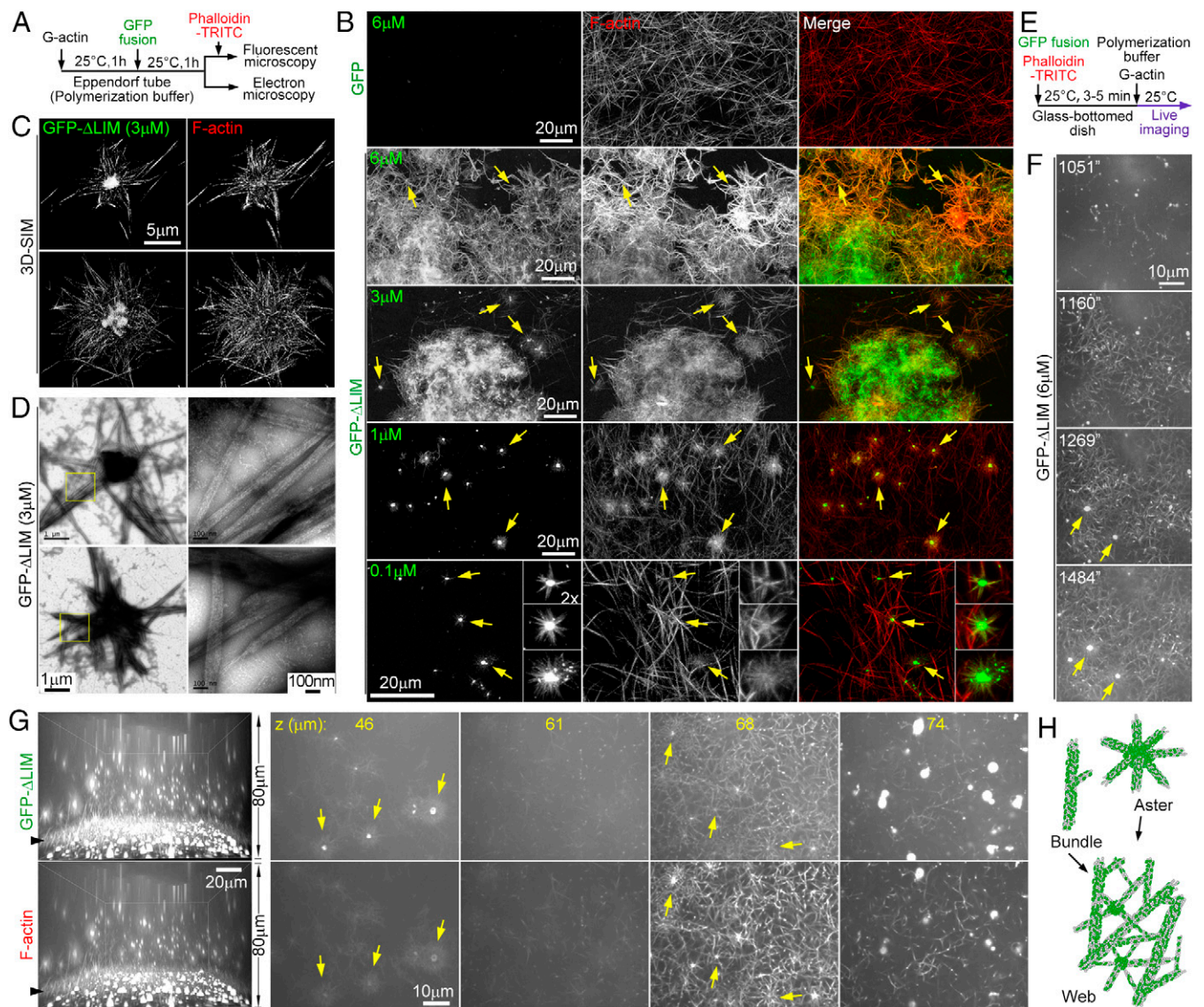
Fig. 2. ΔLIM induces asters and webs of F-actin bundles in vitro. (*A*) Experimental scheme for *B–D*, which is identical to our previous publication (31), for comparison. Actin induced to polymerize for 1 h was mixed with GFP or GFP-ΔLIM as illustrated, at the final actin concentration of 6 μM. Actin filaments were then visualized through EM or fluorescent microscopy. Phalloidin-TRITC (final concentration: 1 μM) was used to label F-actin for fluorescent microscopy. (*B*) Effects of GFP-ΔLIM on F-actin organizations in vitro. GFP served as a negative control. Arrows indicate representative astral structures. Note that a different scale is used for the 0.1-μM sample. A typical batch of purified proteins is shown in *SI Appendix*, Fig. S2A. (*C* and *D*) Detailed morphologies of asters, visualized by 3D-SIM (*C*) or EM with negative staining (*D*). Magnified *Insets* in *D* show actin bundles in the framed regions. (*E*) Experimental scheme for live imaging in *F* and *G*. The final concentration of G-actin was 6 μM. Phalloidin-TRITC (final concentration: 4 μM) was used to label F-actin. (*F*) Representative time-lapse images showing the formation of His-GFP-ΔLIM-induced actin webs. Z-stack images of 1-μm intervals were captured for the GFP autofluorescence to cover a depth of 6 μm close to the bottom of the substratum by spinning disk microscopy at ~3.6-s intervals. The time started immediately after the addition of G-actin. Arrows denote two asters integrated into the web from outside the imaged zone. (*G*) Spatial distribution of ΔLIM-induced actin networks. The same sample was reimaged at a different field of view and at 0.5-μm intervals to cover a z depth of 80 μm after the live imaging in *F*. Shown is the x–z view of 3D reconstructed images and representative z sections (from top to bottom). Arrowheads point to the dense web around the 68-μm position. Also refer to Movie S1. (*H*) Illustrations showing ΔLIM (green)-induced F-actin-based aster, bundle, and web and their relationship.

a rapid fluorescence recovery of the droplets (Fig. 3*E*), indicating their dynamic exchanges of ΔLIM molecules with the milieu. Furthermore, in the presence of polyethylene glycol (PEG), a crowding reagent capable of promoting protein phase separation (19, 24), the droplet formation was observed at as low as 8 nM (*SI Appendix*, Fig. S2C). His-GFP–dematin homologous unfolded (His-GFP-DHU) displayed similar LLPS properties (Fig. 3*F* and *SI Appendix*, Fig. S2 *D* and *E*), whereas neither His-GFP nor His-GFP-VHP were able to phase separate at even 120 μM (Fig. 3*G*), suggesting that the LLPS is mediated through the IDR (18, 20). When we mutated the aromatic amino acids (Fs and Ys), which are known to be critical for LLPS of some IDRs (20, 24, 42), in the DHU region into serine

(S) residues, the resultant mutants, DHU25S and ΔLIM25S, failed to form liquid droplets (Fig. 3*G* and *SI Appendix*, Fig. S2 *A* and *F*). Therefore, ΔLIM can indeed phase separate into liquid droplets through its IDR.

As bacterially expressed His-GFP-abLIM-L is insoluble (31), we investigated whether abLIM-L could form liquid droplets in cells. As cellular abLIM-L is associated with F-actin (Fig. 1*C*) (31), we reasoned that we might need to disrupt the F-actin association to visualize its liquid droplets. As the VHP domain is essential for the F-actin localization of abLIM-L in cells (31), we removed this domain and observed that both GFP-DHU and GFP-ΔVHP formed liquid droplets of rapid protein turn-overs in RPE1 cells (Fig. 3 *H–J*). We found that tagging GFP
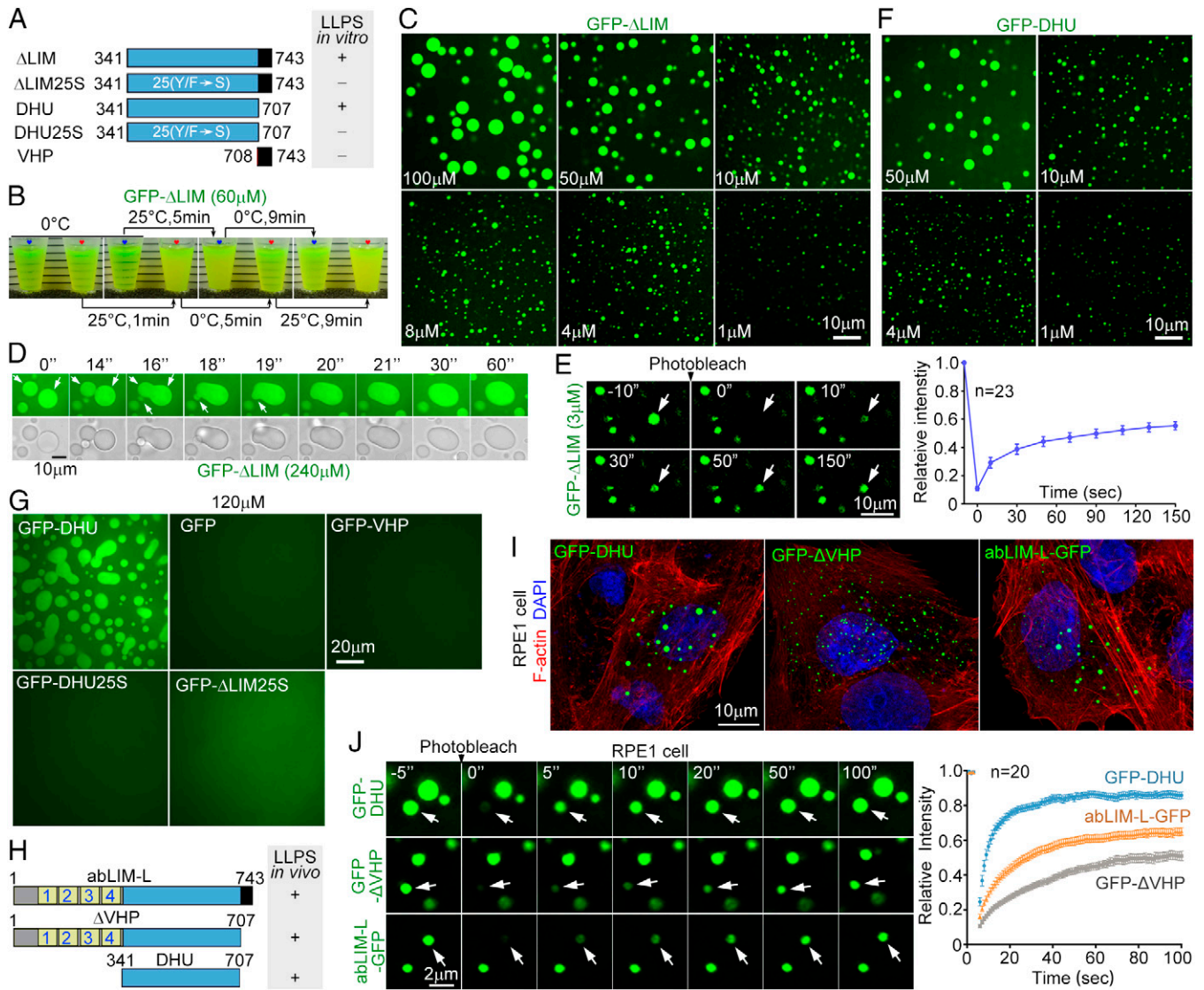
Fig. 3. The abLIM1 undergoes LLPS through its DHU region. (*A*) The abLIM1 mutants used for in vitro assays in *B–G* and a summary of their LLPS properties. (*B*) His-tagged GFP-ΔLIM underwent reversible clear–turbid cycles upon temperature shifts. Two equal aliquots of the protein were treated as depicted and photographed immediately. (*C*) Concentration-dependent LLPS of GFP-ΔLIM. The protein preparation was serially diluted on ice. Each sample was then incubated at 25 °C for 5 min, followed by fluorescent imaging. (*D*) Rapid fusion of GFP-ΔLIM liquid droplets. The protein preparation was incubated at 25 °C for 5 min and live imaged. (*E*) FRAP assays. In the image sequences, arrows indicate a typical droplet before (−10 s) and after (0 s to 150 s) photobleaching. The recovery curve was summarized from 23 droplets. Error bars represent mean ± SEM. (*F*) Concentration-dependent LLPS of His-tagged GFP-DHU. (*G*) His-tagged GFP and GFP-VHP, GFP-DHU25S, and GFP-ΔLIM25S did not undergo LLPS at even 120 μM. (*H* and *I*) GFP-DHU, GFP-ΔVHP, and abLIM-L-GFP formed liquid droplets in cells. RPE1 cells expressing GFP-tagged proteins illustrated in *H* were fixed at 24 h posttransfection and stained with phalloidin-TRITC and DAPI to respectively label actin cytoskeletons and nuclei (*I*). (*J*) The droplets displayed dynamic protein exchanges with the cytosol. FRAP assays were performed with living cells transfected for 24 h as in *I*. In the representative image sequences, arrows indicate droplets before and after photobleaching. Each recovery curve was summarized from 20 droplets. Error bars represent mean ± SEM.

to the C terminus of abLIM-L also inhibited the actin-binding activity of the fusion protein, because abLIM-L-GFP distributed mainly as liquid droplets in 83.6% of RPE1 cells (*n* = 250) (Fig. 3 *I* and *J*). Therefore, abLIM-L is capable of LLPS through its DHU region in vivo.

To understand whether the N-terminal LIM region could affect the LLPS of abLIM1, we purified MBP-His-RFP, MBP-His-RFP-4LIM, and MBP-His-4LIM from *Escherichia coli* (*SI Appendix*, Fig. S3*A*) and added them to preformed liquid droplets of His-GFP-ΔLIM. Rapid disruption of the droplets was observed only when either of the 4LIM fusion proteins was added (Movie S2 and *SI Appendix*, Fig. S3 *B* and *C*). As the LIM domain usually functions by mediating protein interactions (36), we performed coimmunoprecipitation and observed the association of the LIM region with the dematin-homologous region

(*SI Appendix*, Fig. S3*D*). These results suggest that the phase separation property of abLIM1 is self-inhibitory by its N-terminal LIM-containing region.

Liquid Droplets of ΔLIM Massively Polymerize F-actin to Form Asters. How could ΔLIM liquid droplets produce asters of F-actin? We reasoned that, as the astral actin filaments were usually much shorter than sporadic actin filaments in the same samples or even the control (GFP) samples (Fig. 2*B*), ΔLIM liquid droplets might function as actin polymerization centers to directly produce radial actin filaments de novo. To verify this, we monitored liquid droplets of GFP-ΔLIM through live imaging immediately after the addition of G-actin. We used 3 μM GFP-ΔLIM because the droplet size allowed convenient microscopic observations. We observed that numerous hair-like

protrusions continuously grew out of the droplets (Fig. 4A), suggestive of massive nucleation and elongation of F-actin. To confirm this, we included 4 μM phalloidin-TRITC to label F-actin. Although the presence of phalloidin could potentially stabilize actin filaments, it does not influence actin polymerization rate (43) and would thus not interfere with the process of aster formation. Indeed, phalloidin-TRITC rapidly congressed to the outer surface of the droplets within 30 s of the G-actin addition, followed by gradual emergence of GFP-positive F-actin arrays around all the droplets (Fig. 4B and Movie S3). Notably, a portion of the droplets became gradually hollowed during the aster outgrowth (Fig. 4B and Movie S3), suggesting that the astral bundle elongation consumes droplet contents. Consistently, larger droplets produced longer astral actin bundles (Fig. 4 B and C).

Next we examined the effect of Cytochalasin D (CytoD) and Latrunculin A (LatA), drugs that inhibit actin polymerization respectively by preventing actin assembly into the plus end (44) or by sequestering G-actin (45). Asters formed normally in mock-treated samples but were not observed in the presence of 2 μM CytoD or 6 μM LatA in 800 s (Fig. 4D). Only residual actin filaments were observed in the drug-treated samples (Fig. 4D), possibly due to the presence of phalloidin-TRITC. These experiments indicate that the reconstituted asters require actin polymerization.

Aster Formation Is Attributed to LLPS of abLIM1. To clarify whether the aster formation was simply due to directional positioning of abLIM1 molecules on a spherical surface rather than their phase separation, we overexpressed GFP-ΔLIM in HEK293T
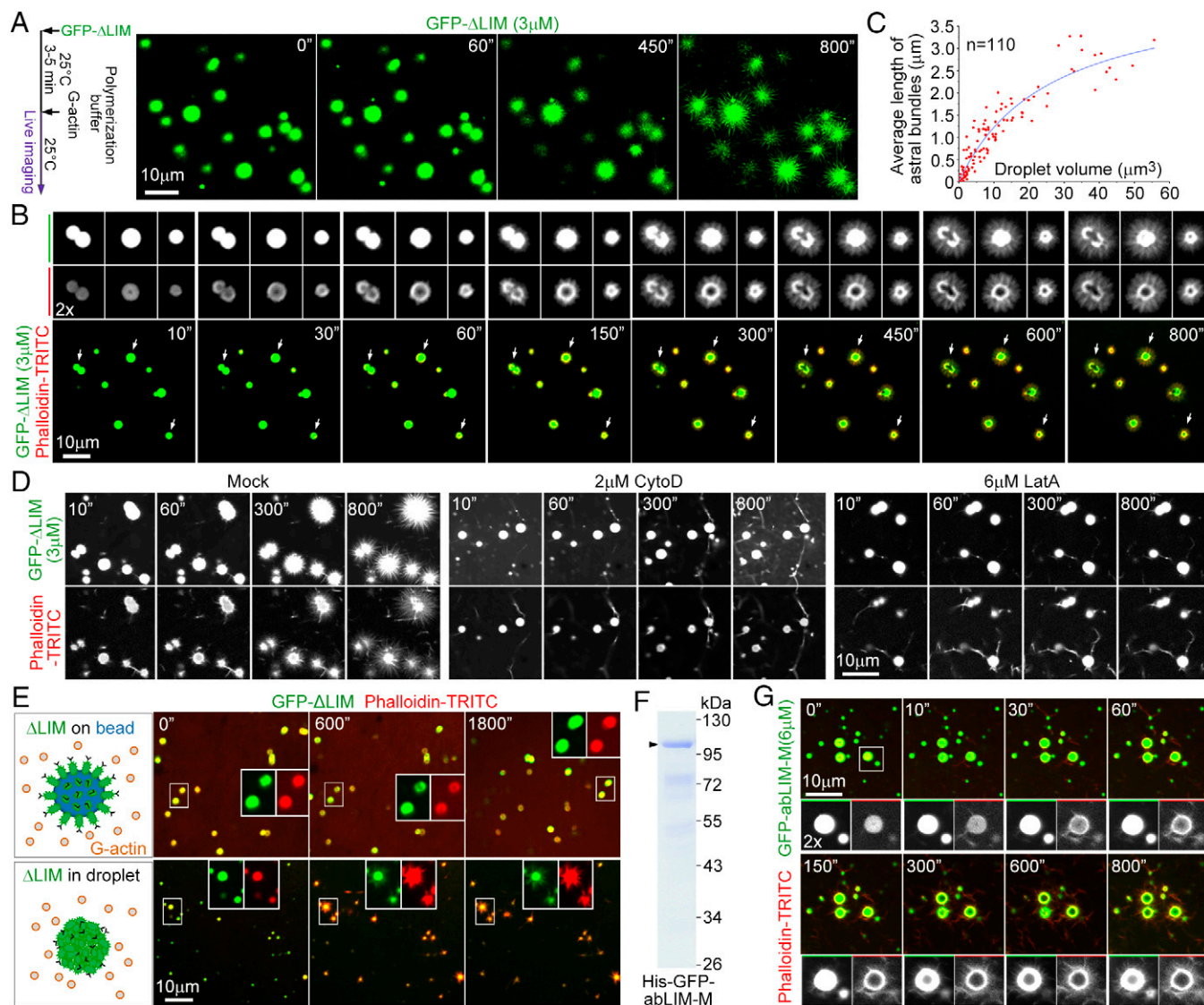

Fig. 4. Liquid droplets of ΔLIM or abLIM-M polymerize and bundle actin filaments into asters. (A and B) Massive actin polymerization from liquid droplets of GFP-ΔLIM. In A, the experiments were performed without phalloidin-TRITC to show that the aster formation is not due to the presence of phalloidin. The experiments in B were performed in the presence of 4 μM phalloidin-TRITC, as depicted in Fig. 2E, to label F-actin. G-actin (final concentration: 6 μM) was added (t = 0 s) into actin polymerization buffer containing preformed liquid droplets of GFP-ΔLIM, followed by live imaging at a single optical section. Three droplets (B, arrows) were magnified to show details. Refer to Movie S3 for detailed processes of B. (C) Positive size–length correlations between GFP-ΔLIM droplets and astral F-actin bundles. The size (volumes) of each droplet and the mean length of its astral bundles were measured from time-lapse images captured at 0 and 30 min, respectively. (D) CytoD and LatA inhibited the aster formation. GFP-ΔLIM liquid droplets were assayed as in B, except that GFP-ΔLIM liquid droplets formed in the presence of dimethyl sulfoxide (mock), CytoD, or LatA were used. (E) F-actin did not grow from GFP-ΔLIM immobilized on beads. GFP-ΔLIM expressed in HEK293T cells for 48 h was concentrated with anti-GFP antibody–conjugated magnetic beads. After the addition of G-actin as in B, the beads were live imaged immediately for 30 min (Top). A parallel sample with preformed liquid droplets of His-GFP-ΔLIM (3 μM) served as a positive control (Bottom). (F and G) Liquid droplets of abLIM-M were also able to generate asters. His-tagged GFP-abLIM-M purified from E. coli (F) formed liquid droplets in the presence of 1% PEG and induced aster formation after the addition of G-actin (G) as in B. A typical droplet (framed) was magnified to show details.

cells and concentrated the protein with anti-GFP antibody-conjugated magnetic beads of ∼1.5 μm in diameter. In this way, ΔLIM molecules on the beads would be oriented with their actin-binding VHP domain pointing out. Direct imaging indicated that GFP fluorescent intensities of the beads were comparable to those of GFP-ΔLIM liquid droplets of similar sizes (Fig. 4E), suggesting similar densities of GFP-ΔLIM molecules on the surface of the beads and the droplets. After the addition of G-actin, however, the beads failed to emanate visible actin filaments, whereas the liquid droplets induced the aster formation (Fig. 4E). Therefore, ΔLIM needs to undergo LLPS for the aster formation.

Although His-GFP-abLIM-L tended to precipitate (31), His-GFP-abLIM-M, the widely expressed major isoform (Fig. 1 *A* and *B*) (30), was soluble (Fig. 4F). We thus examined whether its liquid droplets could also generate asters. We found that GFP-abLIM-M failed to phase separate at even 105 μM, consistent with the inhibitory role of the LIM region (*SI Appendix*, Fig. S3). Nevertheless, it underwent LLPS at 6 μM in the presence of 1% PEG (Fig. 4G). Live imaging indicated that, after the addition of G-actin, the liquid droplets similarly mediated the aster formation (Fig. 4G). Therefore, phase-separated abLIM-M and abLIM-S are able to facilitate local actin polymerization and bundling to form asters.

Formation of F-actin-Based Asters and Webs Requires both DHU and VHP Domains. Next, we investigated critical structural regions of ΔLIM. When actin polymerization assays were performed using liquid droplets of GFP-DHU, no aster formation was observed (Fig. 5A and Movie S4), indicating that both DHU and VHP are required for aster formation. During the imaging, a few F-actin streaks emerged but did not develop into actin networks. Some streaks became weakly decorated by GFP-DHU or associated with liquid droplets (Fig. 5A and Movie S4). Similar F-actin streaks were observed and confirmed to be positive for GFP-DHU when the reactions were performed using the experimental scheme in Fig. 2A (*SI Appendix*, Fig. S4A). EM revealed that the streaks were bundles containing loosely packed actin filaments (*SI Appendix*, Fig. S4B).

We performed a centrifugation-based assay (46) to further verify the F-actin-bundling ability of GFP-DHU. F-actin bundles precipitated from samples containing GFP-DHU (30.0% of total actin levels on average) mildly increased compared to GFP (19.2%) or GFP-VHP (22.0%) but were incomparable to those from samples containing GFP-ΔLIM (67.4%) (Fig. 5B). Consistently, GFP-ΔLIM also apparently coprecipitated with actin bundles (Fig. 5B). Therefore, phase-separated DHU is able to loosely bundle actin filaments, possibly due to weak, multivalent actin-binding abilities of the condensates.

ΔLIM Stimulates Actin Polymerization into Dense Interwoven Networks in Pyrene Actin Polymerization Assays. We next performed pyrene actin polymerization assays (47) to quantitatively assess whether phase-separated ΔLIM functioned to stimulate actin polymerization. We mixed G-actin containing 10% pyrene actin in actin storage buffer with GFP fusion proteins to be examined and incubated briefly at 25 °C to induce LLPS. After the addition of 10× polymerization buffer to initiate actin polymerization, pyrene fluorescence, whose increase indicates actin polymerization (47), was measured with a plate reader (*SI Appendix*, Fig. S4C). GFP-ΔLIM at both 3 μM and 6 μM promoted the polymerization of 6 μM G-actin as compared with GFP (*SI Appendix*, Fig. S4 *D* and *E*). After the completion of biochemical measurements, we performed microscopic examinations.

to directly visualize the fluorescence of pyrene and GFP and observed abundant GFP-positive F-actin webs in the GFP-ΔLIM samples (*SI Appendix*, Fig. S4F), consistent with our earlier observations (Fig. 2). Furthermore, these webs were quite stable even in mounting medium. In comparison, actin filaments in the GFP samples were not visible (*SI Appendix*, Fig. S4F), which is attributed to depolymerization due to the sharp contrast to the phalloidin-TRITC-stained GFP samples (Fig. 2B) (31). The formation of numerous F-actin webs also explains why the polymerization curves of the GFP-ΔLIM samples always oscillated severely, especially at late polymerization phases (*SI Appendix*, Fig. S4 *D* and *E*), because spontaneous orientation changes of the floating webs in the samples would inevitably affect the fluorescence readout of the plate reader.

ΔLIM Promotes Actin Nucleation in an LLPS-Dependent Manner. The rate-limiting step of actin polymerization is nucleation, or the formation of initial actin dimers or trimers (15, 16). To assess whether abLIM1 promoted actin nucleation, we reduced G-actin to 2 μM, a concentration largely precluding spontaneous actin nucleation (47, 48) and thus widely used for assessing nucleator-mediated nucleation activity (49, 50). To our excitement, while the pyrene fluorescence in GFP samples only slightly increased over time, it elevated persistently in 3-μM GFP-ΔLIM samples and plateaued after ∼25 min (Fig. 5C). The average pyrene intensity at the steady state was over that of GFP samples by more than fivefold (Fig. 5C). GFP-tagged DHU or VHP, however, had no apparent effect on the actin polymerization kinetics as compared to GFP (Fig. 5C), again confirming the requirement of both regions. Furthermore, GFP-ΔLIM25S, which did not undergo LLPS (Fig. 3G), was unable to stimulate actin polymerization (Fig. 5C). It also did not bind to or bundle actin filaments (*SI Appendix*, Fig. S4 *A* and *B*).

As we noticed that the addition of 10× polymerization buffer could regionally disrupt the liquid droplets of GFP-ΔLIM, possibly due to the high salt concentrations in the buffer, we omitted the preincubation step (*SI Appendix*, Fig. S4G) and observed a much more rapid initial polymerization rate of 2 μM G-actin in 3 μM GFP-ΔLIM (*SI Appendix*, Fig. S4H vs. Fig. 5C), a hallmark of increased actin nucleation (47, 49, 50). The promotion effect on actin polymerization reduced markedly at reduced GFP-ΔLIM concentrations (*SI Appendix*, Fig. S4H), again correlated with the reduced phase separation ability (Fig. 3C).

Ca^{2+} is commonly supplemented in actin storage buffer to preserve actin monomers due to the poor spontaneous polymerization efficacy of Ca^{2+}-bound G-actin (48). Furthermore, the nucleation efficacy of Ca^{2+}-G-actin is several orders of magnitude lower than its ability to assemble into F-actin (48). Strikingly, when we performed pyrene actin polymerization assays of 2 μM G-actin in the absence of the actin polymerization buffer, that is, in the absence of Mg^{2+} that is commonly known to markedly stimulate actin nucleation and elongation (48), we still observed a gradual but persistent increase of the pyrene fluorescence in GFP-ΔLIM samples over time, in sharp contrast to the expected flat baseline in GFP samples (Fig. 5D). Furthermore, when the G-actin concentration was increased to 6 μM, GFP-ΔLIM induced a rapid elevation of pyrene fluorescence that plateaued after ∼15 min, reaching fluorescent intensities over those in GFP samples by >4.5-fold (Fig. 5D). To distinguish the nucleation activity from the elongation activity, we performed follow-up microscopic examinations. We reasoned that, if the elevated actin polymerization in the GFP-ΔLIM samples was solely due to increased elongation, we would observe extralong F-actin bundles elongated from rare
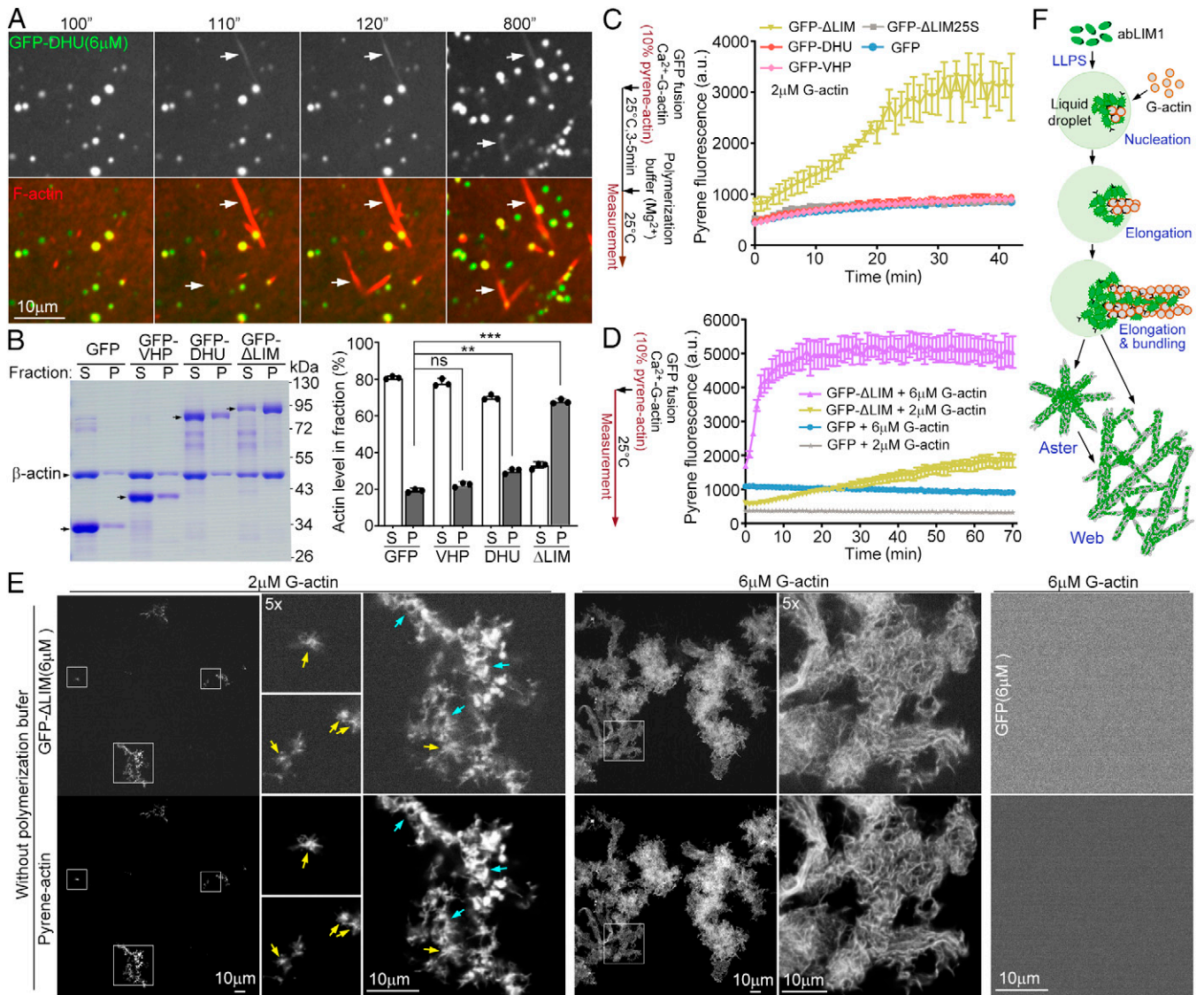
Fig. 5. ΔLIM requires both DHU and VHP for the nucleation and tight bundling of F-actin. (*A*) Liquid droplets of DHU did not induce aster formation. Aster formation assays were performed in 6 μM His-tagged GFP-DHU as depicted in Fig. 2*E*. Arrows indicate typical F-actin streaks. Note that the majority of droplets were free of F-actin, although some appeared to become adhered to F-actin streaks during the imaging. Also see Movie S4. (*B*) DHU mildly bundled actin filaments. G-actin (6 μM) was polymerized in 6 μM His-GFP or His-GFP-tagged VHP, DHU, or ΔLIM. Actin bundles were then precipitated through centrifugation. Proteins in equivalent volumes of the supernatant (S) and pellet (P) fractions from each sample were resolved by SDS/PAGE, followed by Coomassie blue staining. Arrows point to full-length GFP or GFP-tagged proteins. Actin levels relative to the total levels (S + P) in the S or the P fractions were quantified from gels from three independent experiments (mean ± SD). Paired Student's *t* test: ns, no significance (*P* > 0.05); **P < 0.01; ***P < 0.001. (*C*) ΔLIM potently stimulated polymerization of 2 μM G-actin. G-actin (containing 10% pyrene actin) was mixed with the indicated proteins (final concentrations: 3 μM for GFP-ΔLIM or GFP-DHU; 6 μM for GFP, GFP-VHP, or GFP-ΔLIM25S) in Ca²⁺-containing actin storage buffer and incubated as illustrated. After the addition of Mg²⁺-abundant 10× polymerization buffer, polymerization kinetics was monitored with a microplate reader that measured the increased fluorescence of pyrene actin in actin filaments. The curves were summarized from three sets of independent experiments (mean ± SEM). (*D*) ΔLIM effectively stimulated actin polymerization in the absence of polymerization buffer. GFP-ΔLIM or GFP (final concentration: 6 μM) was mixed with G-actin in actin storage buffer (final concentration: 2 or 6 μM), followed immediately by the measurement of pyrene fluorescence. The curves were summarized from three sets of independent experiments (mean ± SEM). (*E*) ΔLIM induced actin polymerization into asters or webs even in the absence of polymerization buffer. After the completion of biochemical measurements in *D*, the samples were mounted into coverslips with mounting medium and directly imaged for GFP and pyrene autofluorescence. Framed regions were magnified to show details. Arrows point to typical asters, with cyan ones pointing to asters containing a hollow center. (*F*) A model illustrating roles of abLIM1. The abLIM1, at least its abLIM-S or abLIM-M isoform, undergoes LLPS to form condensates that nucleate actin and cross-link together actin filaments to generate asters and sporadic bundles, which further develop into webs.

spontaneous actin nuclei; if GFP-ΔLIM had LLPS-dependent nucleation activity, massive numbers of actin filaments would be observed. We found that, in the GFP-ΔLIM samples with 2 μM G-actin, actin filaments were short and mainly radiated from sparse individual or loosely clustered GFP-positive asters (Fig. 5*E*, arrows), confirming the actin nucleation ability of ΔLIM condensates. Some of the asters contained a hollow center void of both GFP and pyrene fluorescence (Fig. 5*E*, cyan arrows), similar to those seen in live imaging (Fig. 4 *B* and *G*). In the GFP-ΔLIM

samples with 6 μM G-actin, we observed abundant GFP-positive actin webs (Fig. 5*E*) similar to those observed in the polymerization buffer (*SI Appendix,* Fig. S4*F*). As actin polymerization completely failed to occur in the GFP samples (Fig. 5 *C* and *D*), the abundant actin webs are probably attributed to both nucleation and elongation effects of ΔLIM condensates.

Taking together our in vitro results (Figs. 2–5), we conclude that the LLPS-induced ΔLIM condensates are capable of potently promoting actin nucleation. The resultant actin filaments are
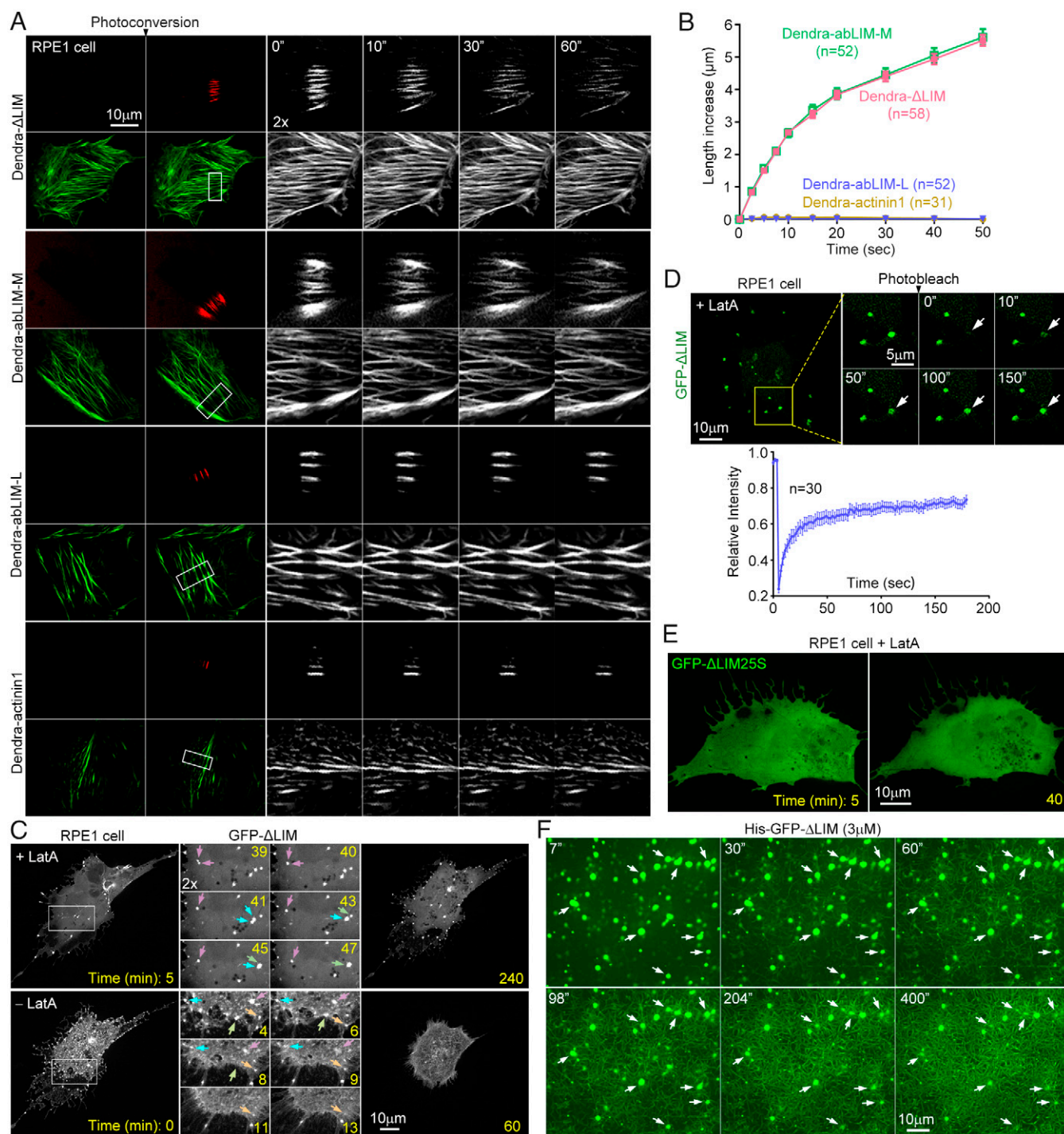
Fig. 6. F-actin-associated ΔLIM and abLIM-M are phase separated in cells. (*A* and *B*) ΔLIM and abLIM-M molecules constantly spread along cellular F-actin bundles. RPE1 cells were transfected to express the indicated Dendra-tagged fusion proteins. A fraction of the proteins in the framed regions was photoconverted to emit red fluorescence, followed by dual-color live imaging (*A*). The length changes of red fluorescence along F-actin bundles over time, relative to the initial (*t* = 0 s) time point, were quantified from 15 cells for each construct (*B*). Data points are presented as mean ± SEM. (*C*) Liquid droplets of GFP-ΔLIM emerged during the disassembly of intracellular F-actin and were rapidly resorbed by repolymerizing F-actin. RPE1 cells transiently expressing GFP-ΔLIM were treated with LatA (1 μg/mL), followed by live imaging (*Top*). Arrows indicate liquid droplets undergoing fusion over time in the framed region. See Movie S5. After imaging for ~4.5 h, LatA was washed out to allow actin repolymerization and the same cell was imaged (*Bottom*). Arrowheads point to representative liquid droplets resorbed over time in the framed region. Also see Movie S6. (*D*) GFP-ΔLIM molecules actively exchanged between liquid droplets and the cytosol. RPE1 cells expressing GFP-ΔLIM were treated with LatA for 1 h to induce liquid droplets, followed by FRAP assays. Arrows indicate dynamic changes of a representative droplet after photobleaching. In the recovery curve, data points are presented as mean ± SEM. (*E*) GFP-ΔLIM25S in cells did not show F-actin association or form liquid droplets upon the LatA treatment. (*F*) Droplet absorptions were observed during the formation of in vitro actin webs. Actin polymerization was performed in 3 μM His-GFP-ΔLIM as depicted in Fig. 2*E* but without phalloidin-TRITC, to exclude potential influence of the drug on actin polymerization and organization. Z-stack GFP fluorescent images were captured for a droplet-abundant area at 1-μm intervals to cover a depth of 6 μm and ~3.6-s intervals by spinning disk microscopy. The time started immediately after the addition of G-actin freshly diluted in polymerization buffer on ice. Arrows denote liquid droplets that were gradually absorbed during the dense F-actin web formation.

then cross-linked together by phase-separated ΔLIM molecules to generate stable asters and sporadic bundles, which further develop into stable webs (Fig. 5*F*).

ΔLIM and abLIM-M Molecules Display Fluidity along F-actin Bundles. As our in vitro assays suggest the importance of LLPS in functions of abLIM1, we investigated whether F-actin-associated abLIM1 molecules in cells were indeed liquid–liquid phase separated. Consistently, when GFP-tagged ΔLIM25S or abLIM25S-M was expressed in U2OS cells, neither displayed clear colocalization with F-actin (*SI Appendix*, Fig. S5 *A* and *B*). Nevertheless, as the 25S mutations might also influence other functions of the DHU region, the results could not be solely attributed to LLPS. We thus sought to address the question more directly.

As condensates with liquid properties should display fluidity, we made use of the photoconvertible property of Dendra, a green fluorescent protein that can be converted into a red fluorescent protein through 405-nm laser irradiation (51). We reasoned that, if we photoconverted F-actin-bound Dendra-abLIM1 molecules in a narrow cellular area, we might be able to assess their fluidity through the spreading of red fluorescence along the actin bundles.

To minimize phototoxicity, we only photoconverted a portion of Dendra molecules in irradiated areas prior to dual-color live imaging (Fig. 6*A*). The photoconversion did not affect the integrity of the F-actin bundles, because their overall architectures were kept unchanged during the imaging, judging by the images in the green fluorescence channel (Fig. 6*A*). Strikingly, the photoconverted molecules of both Dendra-ΔLIM and Dendra-abLIM-M displayed rapid and bidirectional spreading along these bundles, accompanied by gradual reductions in the fluorescent intensity (Fig. 6*A*). Quantifications indicated that the photoconverted ΔLIM and abLIM-M molecules spread along the bundles respectively for a total of 5.5 μm (*n* = 58) and 5.6 μm (*n* = 52) in 50 s, corresponding to an average velocity of 60 nm/s on each side (Fig. 6*B*). Photoconverted Dendra-abLIM-L molecules, however, were almost immobile (Fig. 6 *A* and *B*). We also examined α-actinin, a classical cross-linker that bundles actin filaments by forming rod-shaped antiparallel dimers (52). Consistent with the previous FRAP results (13), photoconverted Dendra-α-actinin1 molecules did not diffuse along F-actin bundles (Fig. 6 *A* and *B*). Therefore, the rapid bidirectional motility of ΔLIM and abLIM-M is not a common feature of actin cross-linkers.

GFP-actin molecules in intracellular actin bundles have a half-time of ~2 min in FRAP assays (13). During this period of time, the boundaries between the bleached and the unbleached regions of the same actin bundles are stationary (13), indicating that bundled actin filaments in cells do not show obvious antiparallel sliding. Consistently, photoconverted Dendra-actin molecules displayed little spreading along F-actin bundles (*SI Appendix*, Fig. S5 *C* and *D*). Therefore, the constant spreading of ΔLIM and abLIM-M molecules along F-actin bundles is attributed to their fluidity, rather than sliding of actin filaments. The lack of motility of abLIM-L is possibly due to a gel-like state of its condensates (20–22) on actin bundles.

Liquid Droplets of ΔLIM and abLIM-M Emerge and Resorb following F-actin Depolymerization and Repolymerization. We further reasoned that, if ΔLIM and abLIM-M molecules in actin bundles were indeed liquid–liquid phase separated, they would emerge as typical liquid droplets following the depolymerization of intracellular actin networks. We thus treated cells expressing GFP-ΔLIM or GFP-abLIM-M with LatA, which induces F-actin disassembly by sequestering G-actin (45), followed by live imaging. Indeed, liquid droplets emerged by 5 min post the

LatA treatment, with their numbers increasing over time (Fig. 6*C*, Movie S5, and *SI Appendix*, Fig. S5*E*). Fusion events were also observed (Fig. 6*C*, Movie S5, and *SI Appendix*, Fig. S5*E*). FRAP assays on the droplets of GFP-ΔLIM indicated their rapid fluorescence recovery (Fig. 6*D*). In contrast, the liquid droplet formation was not observed for GFP-abLIM25S-M and GFP-ΔLIM25S upon the drug treatment (Fig. 6*E* and *SI Appendix*, Fig. S5*F*). Furthermore, although the liquid droplets persistently existed during live imaging of more than 4 h, after the removal of LatA, they became rapidly resorbed by the polymerizing F-actin (Fig. 6*C* and Movie S6). Similar absorptions of GFP-ΔLIM liquid droplets by polymerizing F-actin networks were also observed in vitro (Fig. 6*F*). These results further prove that ΔLIM and abLIM-M molecules can flow along cellular F-actin networks and are indeed liquid–liquid phase separated.

Discussion

We demonstrate that abLIM1, or at least its abLIM-M and abLIM-S isoforms, phase separates into condensates to self-assemble asters and webs of bundled actin filaments. The abLIM1 can undergo LLPS through its DHU region both in vitro and in vivo (Fig. 3 and *SI Appendix*, Fig. S2). Phase-separated abLIM1 condensates, as shown with the abLIM-S-mimicking ΔLIM, cross-link actin filaments together into tightly packed bundles of 58.4-nm average diameter in vitro (Fig. 2 *B–D*) (31). Both the VHP and DHU regions are required for efficient formation of the tight F-actin bundles capable of interconnecting into large webs (Figs. 2 and 5 and *SI Appendix*, Fig. S4). As the VHP domain alone does not display detectable F-actin-binding or F-actin-bundling activity (Fig. 5*B*) (31), it may require the LLPS of DHU to activate. The ΔLIM-induced potent actin polymerization at low (2 μM) G-actin concentration and even in the absence of Mg^{2+} (Fig. 5 *C–E* and *SI Appendix*, Fig. S4) suggests that the actin filaments in ΔLIM-cross-linked bundles are stabilized.

Our results strongly suggest that phase-separated abLIM1 condensates also function as a unique phase separation–dependent actin nucleator. The massive actin polymerization around the liquid droplets of ΔLIM or abLIM-M, but not beads coated with ΔLIM, indicates de novo local nucleation of the astral actin filaments (Fig. 4 and Movie S3). The pyrene actin polymerization results under conditions markedly precluding spontaneous actin nucleation, i.e., with 2-μM G-actin and especially in the absence of Mg^{2+} (Fig. 5 *C–E* and *SI Appendix*, Fig. S4*H*) (48–50) further confirm the nucleation activity. As both the VHP and the phase separation property of DHU are also required for the actin nucleation activity (Figs. 4 and 5), the LLPS of the DHU region might enable VHP multivalency to facilitate the dimerization and trimerization of actin monomers to form actin nuclei (15, 16). Although asters were observed at 0.1 μM ΔLIM in microscopy (Fig. 2*B*), in pyrene actin polymerization assays the ΔLIM-stimulated actin nucleation became obvious at only micromolar concentrations (Fig. 5 *C–E* and *SI Appendix*, Fig. S4*H*) that correspond to its prominent LLPS in vitro (Fig. 3*C*). Such a requirement for LLPS is distinct from canonical actin nucleators formin, spire, and the Arp2/3 complex (7, 15, 16), which are capable of markedly nucleating actin at nanomolar concentrations (47, 49, 50, 53, 54), suggesting that abLIM1 probably functions regionally in cells where it can be sufficiently concentrated to undergo LLPS. Similar to dematin (37), abLIM1 also associates with spectrin (31). Therefore, abLIM1 might be concentrated to the nodes of cortical spectrin networks of nonerythroid cells in ways analogous to dematin in erythrocytes to become phase separated for cortical actin nucleation.

The abLIM1 condensates probably roam along actin filaments to regionally nucleate and cross-link together actin filaments to self-organize elastic, interconnected webs of cortical F-actin bundles for cells to properly resist mechanical tension. The tendency of polymerizing F-actin arrays to consume the liquid droplets (Figs. 4 *B* and *G* and 6*F*) and the positive correlation between the length of astral actin bundles and the size of liquid droplets (Figs. 2*B* and 4 *B* and *C*) suggest liquid-like fluidity of ΔLIM and abLIM-M along F-actin in vitro. Furthermore, the lack of F-actin association of the phase separation–defective mutants ΔLIM25S and abLIM25S-M, the emergence of liquid droplets of abLIM-M and ΔLIM upon actin depolymerization in cells, their resorption into repolymerizing actin cytoskeletons, and their constant spreading along intracellular F-actin bundles (Fig. 6, Movies S5 and S6, and *SI Appendix*, Fig. S5) confirmed that intracellular F-actin-associated abLIM-M and abLIM-S molecules are also liquid–liquid phase separated. Furthermore, our previous studies demonstrate that the dense, interconnected cortical actin networks in RPE1 and U2OS cells become sparse and rich in thick, linear fibers upon the depletion of abLIM1, resulting in membrane blebbing during cell spreading or migration (31). In addition, as abLIM1 is highly enriched at the Z disk of sarcomeres (30, 55), it might also help to construct the actin networks in striated muscle cells by nucleating and cross-linking actin filaments at the Z disk. This is also consistent with the ΔLIM-induced efficient polymerization of Ca^{2+}-G-actin in the absence of Mg^{2+} (Fig. 5 *D* and *E*).

How abLIM1 functions are regulated also remains to be investigated. We found that the LIM-containing region is inhibitory to LLPS of abLIM1, possibly through its interaction with the dematin-homologous ΔLIM region (*SI Appendix*, Fig. S3). Consistently, abLIM-M required the presence of PEG for LLPS (Fig. 4*G*). In contrast, LLPS of LIMD1, a focal adhesion protein, is promoted by multivalent interactions of its N-terminal IDR and C-terminal LIM domains (56), indicating that interplays of LIM domains with IDRs can impact LLPS differently in different proteins. As the LIM domain is a modular protein-binding interface (36), the inhibitory effect of the N-terminal LIM region of abLIM1 on LLPS might be enhanced or abolished through interactions with other proteins or through posttranslational modifications, for example, phosphorylation (30, 56, 57), to fine-tune abLIM1 functions. It is intriguing why abLIM1 contains so many different isoforms (*SI Appendix*, Fig. S1) and expresses abLIM-M widely as the major isoform (Fig. 1 *A* and *B*) but expresses abLIM-L solely in retinal rod cells (30). We indeed found that, although intracellular abLIM-L was also able to undergo LLPS (Fig. 3 *H–J*) and localize on actin bundles (Fig. 1*C*) (31), F-actin-associated abLIM-L molecules appeared immobile and thus differed markedly in this property from abLIM-M and ΔLIM (Fig. 6 *A* and *B*). It is also interesting that LIM-containing regions in some focal adhesion proteins, such as LIMD1 and Zyxin, have recently been shown to function in mechanical sensing (56, 58). Although the F-actin association of abLIM-L is insensitive to mechanical stretching (58), it would be worthwhile to test abLIM-M, considering the distinct diffusion behaviors of the two isoforms along F-actin bundles (Fig. 6 *A* and *B*). Detailed contributions of LIM domain numbers to the LLPS ability and functions of abLIM1 will await future investigations. In addition, abLIM1 paralogues, abLIM2, abLIM3, and dematin, would function to nucleate and bundle actin filaments as well, considering their extensive structural similarities to abLIM1 (30, 32, 35, 59, 60). Future investigations will also be required to clarify these speculations.

Materials and Methods

Plasmids and Oligonucleotides. The full-length complementary DNA (cDNA) for abLIM1 (GenBank accession number MF597763) (39), α-actinin1 (NM_001130004), and β-actin (NM_001101) was cloned from hTERT-RPE1 cells through PCR. The cDNA encoding DHU25S was synthesized and incorporated into the full-length cDNA through CloneEZ seamless cloning technology by Bio-Sune. Their deletion or truncation constructs were generated by PCR. The pEGFP-C2, pDendra-C2, pET28a, and pET-MBP-3C were used to express GFP-, Flag-GFP, Dendra-, His-, and MBP-His-tagged proteins. All constructs were verified by sequencing. siRNAs (Ctrl-i, abL1-i1, and abL1-i2) were ordered from Gene-Pharma, and their sequences were described previously (39).

Antibodies. Primary antibodies used were rabbit anti-β-actin [20536-1-AP, Proteintech; Western blotting (WB) 1:5,000] and rabbit anti-abLIM1 (home-made; Immunofluorescence 1:500 and WB 1:1,000) (39). Secondary antibodies used were donkey anti-rabbit antibody conjugated with Cy3 (Thermo Fisher Scientific; 1:1,000) and horseradish peroxidase–conjugated goat anti-mouse and anti-rabbit antibodies (Thermo Fisher; WB 1:5,000).

Cell Culture, Transfection, and Analysis. The hTERT-RPE1 cells were maintained in Dulbecco's Modified Eagle Medium: Nutrient Mixture F-12 (DMEM/F12) media (Thermo Fisher) supplemented with 10% fetal bovine serum (FBS), 100 units/mL penicillin, 100 μg/mL streptomycin, and 10 μg/mL Hygromycin B (Invitrogen). HEK293T, U2OS, NIH 3T3, and IMCD3 cells were maintained in DMEM supplemented with the same amount of FBS, penicillin, and streptomycin. For plasmid transfection, cells were transfected at ~70% confluency with Lipofectamine 2000 (Thermo Fisher) or polyethylenimines (Polysciences 23966-2). For transfection of siRNAs (GenePharma), cells were transfected with Lipofectamine RNAiMAX (Thermo Fisher) as described previously, and harvested after 48 h (31, 39).

Cells were lysed for immunoblotting or coimmunoprecipitation, fixed for fluorescent staining and imaging, or live imaged. See *SI Appendix, Extended Methods* for details.

Protein Expression and Purification. His-tagged proteins used for in vitro assays were expressed in *E. coli* and affinity purified. See *SI Appendix, Extended Methods* for details.

Protein Turbidity Assay. Purified His-GFP-ΔLIM or His-GFP-DHU was equally divided into two differently marked 1.5-mL Eppendorf tubes on ice and shifted alternately between 0 °C and 25 °C as depicted (Fig. 3*B* and *SI Appendix*, Fig. S2*D*). The first elapsed time was the time when the sample incubated at 25 °C became obviously turbid, whereas the second or third elapsed time was the time when the sample shifted from 25 °C to 0 °C became obviously clear. Aging was obvious because a longer time was required for the samples to become clear after each cycle, and the samples became irreversible after a few cycles. The pair of tubes were photographed side by side with a digital camera (Sony, DSC-RX100) against a striped white background to examine the transparency of the protein samples.

In Vitro Phase Separation Assay. Purified proteins were diluted to the required concentrations into PBS on ice. After incubation at 25 °C for 5 min, 3 μL of each protein were loaded into a chamber, made by sticking a glass coverslip with two pieces of double-sided adhesive tape onto a slide or 35-mm glass-bottom dish (Cellvis, D35-20-1.5-N), and imaged immediately using a spinning disk confocal microscope (UltraVIEW VoX, PerkinElmer). To monitor spontaneous droplet fusions, single-section live imaging was performed at 0.5-s intervals with the spinning disk confocal microscope.

FRAP assays were performed following the FRAP wizard in Leica SP8 confocal microscope. Briefly, His-GFP-ΔLIM was diluted to 3 μM on ice and loaded onto a 29-mm glass-bottom dish (Cellvis, D29-14-1.5-N) at room temperature. Liquid droplets sitting at the bottom of the substratum were then photobleached using the 488-nm laser with 100% power three times, for 1.29 s each. The postbleaching images were acquired at 20-s intervals at 0.5% laser power for ~5 min.

In Vitro Actin Polymerization. Actin polymerization assays were performed with 2 or 6 μM G-actin. Purified His-GFP or His-GFP-tagged abLIM1 constructs were mixed with preformed actin filaments (Fig. 2 *A–D* and *SI Appendix*, Fig. S4 *A and B*) to examine their effects on F-actin organization or with G-actin and the

polymerization buffer, followed by live imaging (Figs. 2 *E–G*, 4, and 5*A* and *SI Appendix,* Fig. S2*B*) to visualize actin polymerization or by centrifugation and SDS/PAGE (Fig. 5*B*) to examine levels of F-actin bundles. Pyrene actin polymerization assays were performed following the manufacturer's protocol (Cytoskeleton) with minor modifications. See *SI Appendix, Extended Methods* for details.

Quantification and Statistical Analysis. The average length of astral bundles at $t = 30$ min and the initial volume of the corresponding liquid droplets (i.e., at $t = 0$ min) were measured with ImageJ software (NIH) (Fig. 4*C*). The length increase of photoconverted red fluorescence of Dendra along stress fibers (Fig. 6*B* and *SI Appendix,* Fig. S5*D*) was measured using the polyline tool of LAS X software (Leica). Quantification results are presented as mean ± SEM or mean ± SD. Statistical analyses were performed using GraphPad Prism 8.

Data Availability. All study data are included in the article and/or supporting information.

Author affiliations: [a]State Key Laboratory of Cell Biology, Shanghai Institute of Biochemistry and Cell Biology, Center for Excellence in Molecular Cell Science, Chinese Academy of Sciences, Shanghai 200031, China; [b]University of Chinese Academy of Sciences, Beijing 100049, China; [c]School of Life Science and Technology, ShanghaiTech University, Shanghai 201210, China; [d]National Laboratory of Biomacromolecules, Institute of Biophysics, Chinese Academy of Sciences, Beijing 100101, China; and [e]School of Life Science, Hangzhou Institute for Advanced Study, University of Chinese Academy of Sciences, Hangzhou 310024, China

1. V. Bennett, A. J. Baines, Spectrin and ankyrin-based pathways: Metazoan inventions for integrating cells into tissues. *Physiol. Rev.* **81**, 1353–1392 (2001).
2. A. J. Baines, The spectrin-ankyrin-4.1-adducin membrane skeleton: Adapting eukaryotic cells to the demands of animal life. *Protoplasma* **244**, 99–131 (2010).
3. D. V. Köster, S. Mayor, Cortical actin and the plasma membrane: Inextricably intertwined. *Curr. Opin. Cell Biol.* **38**, 81–89 (2016).
4. J. Y. Tinevez *et al.*, Role of cortical tension in bleb growth. *Proc. Natl. Acad. Sci. U.S.A.* **106**, 18581–18586 (2009).
5. P. Chugh *et al.*, Actin cortex architecture regulates cell surface tension. *Nat. Cell Biol.* **19**, 689–697 (2017).
6. G. Salbreux, G. Charras, E. Paluch, Actin cortex mechanics and cellular morphogenesis. *Trends Cell Biol.* **22**, 536–545 (2012).
7. C. T. Skau, C. M. Waterman, Specification of architecture and function of actin structures by actin nucleation factors. *Annu. Rev. Biophys.* **44**, 285–310 (2015).
8. K. Gowrishankar *et al.*, Active remodeling of cortical actin regulates spatiotemporal organization of cell surface molecules. *Cell* **149**, 1353–1367 (2012).
9. F. Eghiaian, A. Rigato, S. Scheuring, Structural, mechanical, and dynamical variability of the actin cortex in living cells. *Biophys. J.* **108**, 1330–1340 (2015).
10. K. Xu, H. P. Babcock, X. Zhuang, Dual-objective STORM reveals three-dimensional filament organization in the actin cytoskeleton. *Nat. Methods* **9**, 185–188 (2012).
11. D. Li *et al.*, Extended-resolution structured illumination imaging of endocytic and cytoskeletal dynamics. *Science* **349**, aab3500 (2015).
12. Y. Zhang *et al.*, In vivo dynamics of the cortical actin network revealed by fast-scanning atomic force microscopy. *Microscopy (Oxf.)* **66**, 272–282 (2017).
13. P. Hotulainen, P. Lappalainen, Stress fibers are generated by two distinct actin assembly mechanisms in motile cells. *J. Cell Biol.* **173**, 383–394 (2006).
14. S. Tojkander *et al.*, A molecular pathway for myosin II recruitment to stress fibers. *Curr. Biol.* **21**, 539–550 (2011).
15. E. S. Chhabra, H. N. Higgs, The many faces of actin: Matching assembly factors with cellular structures. *Nat. Cell Biol.* **9**, 1110–1121 (2007).
16. K. G. Campellone, M. D. Welch, A nucleator arms race: Cellular control of actin assembly. *Nat. Rev. Mol. Cell Biol.* **11**, 237–251 (2010).
17. M. Bovellan *et al.*, Cellular control of cortical actin nucleation. *Curr. Biol.* **24**, 1628–1635 (2014).
18. V. N. Uversky, Intrinsically disordered proteins in overcrowded milieu: Membrane-less organelles, phase separation, and intrinsic disorder. *Curr. Opin. Struct. Biol.* **44**, 18–30 (2017).
19. L. P. Bergeron-Sandoval, N. Safaee, S. W. Michnick, Mechanisms and consequences of macromolecular phase separation. *Cell* **165**, 1067–1079 (2016).
20. S. F. Banani, H. O. Lee, A. A. Hyman, M. K. Rosen, Biomolecular condensates: Organizers of cellular biochemistry. *Nat. Rev. Mol. Cell Biol.* **18**, 285–298 (2017).
21. H. Zhang *et al.*, Liquid-liquid phase separation in biology: Mechanisms, physiological functions and human diseases. *Sci. China Life Sci.* **63**, 953–985 (2020).
22. Y. Shin, C. P. Brangwynne, Liquid phase condensation in cell physiology and disease. *Science* **357**, eaaf4382 (2017).
23. A. Hernández-Vega *et al.*, Local nucleation of microtubule bundles through tubulin concentration into a condensed tau phase. *Cell Rep.* **20**, 2304–2312 (2017).
24. H. Jiang *et al.*, Phase transition of spindle-associated protein regulate spindle apparatus assembly. *Cell* **163**, 108–122 (2015).
25. J. B. Woodruff *et al.*, The centrosome is a selective condensate that nucleates microtubules by concentrating tubulin. *Cell* **169**, 1066–1077.e10 (2017).
26. M. R. King, S. Petry, Phase separation of TPX2 enhances and spatially coordinates microtubule nucleation. *Nat. Commun.* **11**, 270 (2020).
27. L. B. Case, X. Zhang, J. A. Ditlev, M. K. Rosen, Stoichiometry controls activity of phase-separated clusters of actin signaling proteins. *Science* **363**, 1093–1097 (2019).
28. X. Su *et al.*, Phase separation of signaling molecules promotes T cell receptor signal transduction. *Science* **352**, 595–599 (2016).
29. M. L. Zeng *et al.*, Reconstituted postsynaptic density as a molecular platform for understanding synapse formation and plasticity. *Cell* **174**, 1172–1187.e16 (2018).
30. D. J. Roof, A. Hayes, M. Adamian, A. H. Chishti, T. Li, Molecular characterization of abLIM, a novel actin-binding and double zinc finger protein. *J. Cell Biol.* **138**, 575–588 (1997).
31. G. Li *et al.*, abLIM1 constructs non-erythroid cortical actin networks to prevent mechanical tension-induced blebbing. *Cell Discov.* **4**, 42 (2018).
32. L. Chen, Z. G. Jiang, A. A. Khan, A. H. Chishti, C. J. McKnight, Dematin exhibits a natively unfolded core domain and an independently folded headpiece domain. *Protein Sci.* **18**, 629–636 (2009).
33. R. Khanna *et al.*, Headpiece domain of dematin is required for the stability of the erythrocyte membrane. *Proc. Natl. Acad. Sci. U.S.A.* **99**, 6637–6642 (2002).
34. D. Vardar *et al.*, Villin-type headpiece domains show a wide range of F-actin-binding affinities. *Cell Motil. Cytoskeleton* **52**, 9–21 (2002).
35. A. P. Rana, P. Ruff, G. J. Maalouf, D. W. Speicher, A. H. Chishti, Cloning of human erythroid dematin reveals another member of the villin family. *Proc. Natl. Acad. Sci. U.S.A.* **90**, 6651–6655 (1993).
36. J. L. Kadrmas, M. C. Beckerle, The LIM domain: From the cytoskeleton to the nucleus. *Nat. Rev. Mol. Cell Biol.* **5**, 920–931 (2004).
37. I. Koshino, N. Mohandas, Y. Takakuwa, Identification of a novel role for dematin in regulating red cell membrane function by modulating spectrin-actin interaction. *J. Biol. Chem.* **287**, 35244–35250 (2012).
38. Y. Lu *et al.*, Gene disruption of dematin causes precipitous loss of erythrocyte membrane stability and severe hemolytic anemia. *Blood* **128**, 93–103 (2016).
39. J. Cao *et al.*, miR-129-3p controls cilia assembly by regulating CP110 and actin dynamics. *Nat. Cell Biol.* **14**, 697–706 (2012).
40. Y. Guo *et al.*, Visualizing intracellular organelle and cytoskeletal interactions at nanoscale resolution on millisecond timescales. *Cell* **175**, 1430–1442.e17 (2018).
41. Z. J. Huang, R. P. Haugland, W. M. You, R. P. Haugland, Phallotoxin and actin binding assay by fluorescence enhancement. *Anal. Biochem.* **200**, 199–204 (1992).
42. J. Wang *et al.*, A molecular grammar governing the driving forces for phase separation of prion-like RNA binding proteins. *Cell* **174**, 688–699.e16 (2018).
43. J. E. Estes, L. A. Selden, L. C. Gershman, Mechanism of action of phalloidin on the polymerization of muscle actin. *Biochemistry* **20**, 708–712 (1981).
44. J. A. Cooper, Effects of cytochalasin and phalloidin on actin. *J. Cell Biol.* **105**, 1473–1478 (1987).
45. M. Coué, S. L. Brenner, I. Spector, E. D. Korn, Inhibition of actin polymerization by latrunculin A. *FEBS Lett.* **213**, 316–318 (1987).
46. T. A. Fulga *et al.*, Abnormal bundling and accumulation of F-actin mediates tau-induced neuronal degeneration in vivo. *Nat. Cell Biol.* **9**, 139–148 (2007).
47. J. B. Zuchero, In vitro actin assembly assays and purification from *Acanthamoeba*. *Methods Mol. Biol.* **370**, 213–226 (2007).
48. L. S. Tobacman, E. D. Korn, The kinetics of actin nucleation and polymerization. *J. Biol. Chem.* **258**, 3207–3214 (1983).
49. H. Y. Ho, R. Rohatgi, A. M. Lebensohn, M. W. Kirschner, In vitro reconstitution of cdc42-mediated actin assembly using purified components. *Methods Enzymol.* **406**, 174–190 (2006).
50. E. Derivery, A. Gautreau, Assaying WAVE and WASH complex constitutive activities toward the Arp2/3 complex. *Methods Enzymol.* **484**, 677–695 (2010).
51. N. G. Gurskaya *et al.*, Engineering of a monomeric green-to-red photoactivatable fluorescent protein induced by blue light. *Nat. Biotechnol.* **24**, 461–465 (2006).
52. B. Sjöblom, A. Salmazo, K. Djinović-Carugo, Alpha-actinin structure and regulation. *Cell. Mol. Life Sci.* **65**, 2688–2701 (2008).
53. M. E. Quinlan, J. E. Heuser, E. Kerkhoff, R. D. Mullins, *Drosophila* Spire is an actin nucleation factor. *Nature* **433**, 382–388 (2005).
54. F. Li, H. N. Higgs, The mouse Formin mDia1 is a potent actin nucleation factor regulated by autoinhibition. *Curr. Biol.* **13**, 1335–1340 (2003).
55. D. Frank, N. Frey, Cardiac Z-disc signaling network. *J. Biol. Chem.* **286**, 9897–9904 (2011).
56. Y. Wang *et al.*, LIMD1 phase separation contributes to cellular mechanics and durotaxis by regulating focal adhesion dynamics in response to force. *Dev. Cell* **56**, 1313–1325.e7 (2021).
57. P. Schneider *et al.*, Identification of a novel actin-dependent signal transducing module allows for the targeted degradation of GLI1. *Nat. Commun.* **6**, 8023 (2015).
58. X. Sun *et al.*, Mechanosensing through direct binding of tensed F-actin by LIM domains. *Dev. Cell* **55**, 468–482.e7 (2020).
59. M. Krupp, A. Weinmann, P. R. Galle, A. Teufel, Actin binding LIM protein 3 (abLIM3). *Int. J. Mol. Med.* **17**, 129–133 (2006).
60. T. Barrientos *et al.*, Two novel members of the ABLIM protein family, ABLIM-2 and -3, associate with STARS and directly bind F-actin. *J. Biol. Chem.* **282**, 8393–8403 (2007).